Disruption of Wave-associated Rac GTPase-activating Protein (Wrp) Leads to Abnormal Adult Neural Progenitor Migration Associated with Hydrocephalus[*]

Il Hwan Kim[‡], Benjamin R. Carlson[‡], Clifford C. Heindel[‡], Hyun Kim[§], and Scott H. Soderling[‡1]

From the [‡]Department of Cell Biology, Duke University Medical School, Durham, North Carolina 27710 and the [§]Department of Anatomy, College of Medicine, Korea University, Brain Korea 21, Seoul 136-705, Korea

Background: Obstructive hydrocephalus results from blockage of the cerebral aqueduct, a poorly understood process.
Results: Deletion of Wrp leads to mis-migration of postnatal neural progenitors, tissue disruption, and blockage of the cerebral aqueduct.
Conclusion: Wrp is critical for normal neural progenitor migration out of the subventricular zone.
Significance: Obstructive hydrocephalus may arise as a result of abnormal neural progenitor properties.

Hydrocephalus is the most common developmental disability and leading cause of brain surgery for children. Current treatments are limited to surgical intervention, as the factors that contribute to the initiation of hydrocephalus are poorly understood. Here, we describe the development of obstructive hydrocephalus in mice that are null for *Wrp* (*Srgap3*). *Wrp* is highly expressed in the ventricular stem cell niche, and it is a gene required for cytoskeletal organization and is associated with syndromic and psychiatric disorders in humans. During the postnatal period of progenitor cell expansion and ventricular wall remodeling, loss of *Wrp* results in the abnormal migration of lineage-tagged cells from the ventricular region into the corpus callosum. Within this region, mutant progenitors appear to give rise to abnormal astroglial cells and induce periventricular lesions and hemorrhage that leads to cerebral aqueductal occlusion. These results indicate that periventricular abnormalities arising from abnormal migration from the ventricular niche can be an initiating cause of noncommunicating hydrocephalus.

Hydrocephalus affects one in every 500 live births (ninds.nih.gov). Obstructive (or noncommunicating) hydrocephalus occurs when the flow of CSF[2] is blocked by stenosis of the cerebral aqueduct or by obstacles such as tumors or hemorrhage (1). Subsequently, it is assumed that increased CSF pressure causes distension of the lateral ventricles, leading to damage within adjacent brain tissues. However, the initial processes or factors that give rise to aqueductal obstruction are poorly defined, making it difficult to understand the detailed etiology of this disorder. Moreover, many of the current genetic animal models of hydrocephalus are nonobstructive, including Ift88 (2), Hy3 (3), Mdnah5 (4), E2F-5 (5), and Celsr2/Celsr3 (6), and are related to ciliary defects affecting the CSF circulating system. However, the population of patients that have ciliary defects, such as primary ciliary dyskinesia, is very rare (1 in 20,000–30,000) when compared with that of hydrocephalus (1 in 500), suggesting the existence of other unknown etiological factors.

Wrp (WAVE-associated Rac GTPase-activating protein, also known as srGAP3 or MEGAP) is one member of the srGAP family (Slit-Robo Rho GTPase-activating proteins) (7–10). *Wrp* is associated with multiple neurodevelopmental disorders and regulates the actin cytoskeleton by forming a signaling complex with WAVE-1 to regulate its activation downstream of the small GTPases Rac (11, 12). *Wrp* is one of several genes that are commonly deleted in 3p-syndrome, a form of syndromic mental retardation. The phenotypic range of this syndrome is variable but can encompass brain anomalies with enlarged lateral ventricles (13).

Lining the lateral ventricles is the subventricular zone (SVZ) and ependyma, which form a specialized stem cell niche in rodents and humans from which newborn cells are continuously produced and migrate into the olfactory bulb (OB) through the rostral migratory stream (RMS) (14–16). It has been reported that a subpopulation of GFAP-positive B-type cells divide and subsequently differentiate to give rise to migratory neuroblasts (17–19). These cells retain their progenitor characteristics only when they reside in the niche (15), suggesting that the special environmental conditions there are essential for maintaining stem cell properties. Recent studies have proposed that the multipotent neural progenitors that escape from the ventricular stem cell niche are at risk for malignant transformation and have a high potential to form gliomas (20–23). In rodents, the amount of progenitor cell production in the ventricular niche at the perinatal stage is 40-fold higher than that of the adult (24). Thus, the collective evidence implies that that the perinatal period could be particularly sensitive to migration abnormalities from the SVZ niche, which may lead to

2 The abbreviations used are: CSF, cerebral spinal fluid; SVZ, subventricular zone; OB, olfactory bulb; RMS, rostral migratory stream; DCX, doublecortin; GFAP, glial fibrillary acidic protein; CC, corpus callosum; LV, lateral ventricle; APP, amyloid precursor protein; IHC, immunohistochemistry; AraC, arabinofuranosyl cytidine.

progenitor migration into neighboring brain regions and mis-differentiation.

Here, we describe the development of enlarged ventricles and obstructive hydrocephalus in *Wrp*-deficient mice that is associated with abnormalities in Nestin^{+} cells of the subventricular region. We find that *Wrp* mRNA and protein are highly expressed in progenitor cells of the stem cell niche in the SVZ, ependyma, RMS, and OB. *Wrp* knock-out mice develop massive disruptions within the brain, predominantly in the neighboring corpus callosum (CC) where abnormally located progenitor cells are observed. Viral lineage tracing and conditional genetic deletion of *Wrp* in Nestin^{+} cells indicate that the mislocated cells originate as progenitor cells that mis-migrate from the ventricular zone. Subsequently, the CC disruption leads to cystic cavities and debris formation. The debris appears to be released into the ventricular space, resulting in blockage of the aqueduct and ultimately leading to obstructive hydrocephalus. Together, these findings suggest that abnormalities in the neural stem cell niche can be an initiating factor for the pathophysiology of hydrocephalus.

EXPERIMENTAL PROCEDURES

Animals—*Wrp* null mice (25) were generated by crossing the floxed allele into a CMV-Cre transgene line and then backcrossed >8 times with C57BL/6 before use. *Wrp* conditional knock-out mice (25) were crossed with Nestin-CreER mouse line to conditionally delete *Wrp* in Nestin-positive cells (26). Littermate mice from heterozygous parents were used for all experiments. Both male and female mice were analyzed, with no differences noted between sexes. All mice were housed in the Division of Laboratory Animal Resources facilities at Duke University, and all procedures were approved by the Duke University Institutional Animal Care and Use Committee and were in accordance with National Institutes of Health guidelines.

In Situ Hybridization Histochemistry—*In situ* hybridization histochemistry was performed as described previously (27). Briefly, frozen developing rat brains (P3, P7, P12, P18, and P25) were sectioned (12 μm) on a cryostat (Leica CM 3000), thaw-mounted onto gelatin-coated glass slides, allowed to dry, and stored at −20 °C until use. Sections were fixed in 4% paraformaldehyde, washed with phosphate-buffered saline (PBS), and acetylated with 0.25% acetic anhydrides (Sigma) in 0.1 M triethanolamine, 0.9% NaCl (pH 8.0). The antisense riboprobes for *Wrp* were prepared from pGEM T-EASY (Promega) vectors containing *Wrp* (GenBank[TM] accession number XM_575637, nucleotides 2159–2706) using an *in vitro* transcription system (Promega) in the presence of γ-^{35}S-UTP (Amersham Biosciences). The sections were then hybridized overnight with radiolabeled probe (1.2×10^6 cpm/slide) and washed sequentially in $2\times, 1\times, 0.5\times$, and in $0.1\times$ SSC with 160 μl of 2.5 M DTT for 30 min each at 62 °C. Finally, the sections were dehydrated, air-dried, and exposed to x-ray film (Biomax MR, Eastman Kodak Co.).

Immunohistochemistry—Mice were deeply anesthetized with isoflurane and then perfused transcardially with Tris-buffered saline (TBS) (pH 7.4) containing 25 units/ml heparin, followed by 4% paraformaldehyde in TBS. Brains were removed, postfixed overnight at 4 °C in the same fixative, and then cryo-

protected with 30% sucrose in TBS. Brains were cut by cryostat (Leica CM 3000) and stored at −20 °C until use. Sections were blocked for 4 h with TBS containing 5% normal goat serum and 0.2% Triton X-100 and then incubated with the following: guinea pig anti-DCX antibody (1:2,000; Millipore); mouse anti-Nestin monoclonal antibody (1:200; BD Biosciences); mouse anti-EphA2 monoclonal antibody (1:200; Sigma); mouse anti-GFAP monoclonal antibody (1:500; BD Biosciences); mouse anti-Alzheimer precursor protein A4 (APP) monoclonal antibody (1:200, clone 22C11; Millipore); rabbit anti-AQP1 polyclonal antibody (1:2,000; Alpha Diagnostics); rabbit anti-red fluorescent protein polyclonal antibody (1:1,000; Rockland); or rabbit anti-Ki-67 polyclonal antibody (1:200; Abcam) overnight at 4 °C. For rat anti-BrdU monoclonal antibody (1:1,000; Accurate Chemical & Scientific Corp.) and rabbit anti-WRP polyclonal antibody (VO112), antigen retrieval procedure was carried out before the immunostainings. After washing three times with TBST (TBS containing 0.2% Triton X-100), sections were incubated with Alexa Fluor® 488 IgG (1:500; Molecular Probes) or Alexa Fluor® 555 IgG (1:500) for 1 h at room temperature. Sections were counterstained with a 4′,6-diamidino-2-phenylindole solution (DAPI; Sigma). After washing four times, the sections were coverslipped with aqueous mounting medium (Calbiochem) and observed under a confocal microscope (LSM 710; Zeiss) or fluorescent microscope (DMRA2; Leica). To reduce variations, all the tissues in one set of experiments were processed at the same time.

Bromodeoxyuridine (BrdU) Treatment—To identify newly generated cells in SVZ and RMS, 200 mg/kg BrdU (Sigma) in saline solution was injected intraperitoneally into P40 mice. Four days after single administration of BrdU, mice were perfused, and brains were processed for immunohistochemical assays.

Magnetic Resonance Imaging Morphometric Analysis—Magnetic resonance imaging was performed as described previously (28) on a 9.4-tesla Oxford vertical bore magnet with a GE EXCITE Console (EPIC 11.0) that has been specially adapted for magnetic resonance microscopy. We used a 14-mm diameter RF solenoid coil. Images were acquired using a three-dimensional gradient recalled echo protocol with echo time (TE) = 3.4 ms, repetition time (TR) = 50 ms, band width (BW) = 62.5 kHz, and a flip angle of 60°. Images were acquired with a field of view of $22 \times 11 \times 11$ mm and a matrix size of $512 \times 256 \times 256$, resulting in an isotropic resolution of 43 μm. The brain images were manually segmented for ventricles using both ImageJ (National Institutes of Health) and MetaMorph (Molecular Devices) software suites. The ventricle system was segmented as four discrete systems comprised of the left lateral ventricle, the right lateral ventricle, the third ventricle and cerebral aqueduct, and the fourth ventricle. Manual segmentation was possible due to the high contrast between brain tissues and the cerebral spinal fluid within the ventricles. Two-dimensional area ratios between the brain section and the ventricles were made using the ImageJ software. Three-dimensional reconstructions were produced using the MetaMorph software.

CSF Circulation Assay—P9, P12, and P40 mice were anesthetized with intraperitoneal injection of ketamine (150 mg/kg)/ xylazine (15 mg/kg). The 30-gauge dental needle (connected to

microdriver with a 10-μl Hamilton syringe) was positioned at 0.1 mm posterior and 1.0 mm lateral to the bregma using a stereotaxic instrument (David Kopf Instruments). Five percent of Evans blue dye in PBS (2 μl for P9 mice, 3 μl for P12, and 5 μl for P40 mice) was infused slowly into right side of the LV (1 μl/min). Mice were sacrificed 1 h after the infusion, and whole brains were removed and then fixed in 4% paraformaldehyde in TBS for 72 h. Following coronal serial section, the distribution of the dye was traced from LVs to spinal cord.

Fluorescent Nano-bead Tracing—P5 mice were anesthetized by hypothermia and placed on an inverted illuminating platform. One microliter of 10% nano-beads (FluoSpheres®, red-orange, 40 nm diameter; Invitrogen) were infused into the lateral ventricle by a Hamilton syringe. At P12, the mice were perfused and post-fixed followed by cryo-protection as described under "Immunohistochemistry." The hemispheres opposite to the injected side were sagittally cut (40 μm thick) and counterstained with DAPI followed by mounting onto slides. Eighty planes of images (0.5 μm gap) were captured from each section to create a z-stack by confocal microscopy (LSM 710; Zeiss), and the bead densities in the ependyma and the CC area were visualized by ZEN software (Zeiss).

Lentiviral Infection and Tracing—The lentiviral and packaging vectors (FCtdTW, VSVg, and Δ8.9) were generously provided from Dr. Michael Ehlers (Duke University), and the viruses were purified as described before (29). One microliter of lentivirus expressing tdTomato was infused into the lateral ventricle of P3 mice as described under "Fluorescent Nano-bead Tracing." At P12, the mice were perfused to prepare sections (40 μm thick) for following immunohistochemical assays as described above. The sections were immunostained by anti-Nestin antibody, and by anti-red fluorescent protein antibody for amplifying the tdTomato signals. Resulting sections were observed by confocal microscopy (LSM 710; Zeiss).

Nissl and H&E Staining—The brain sections were mounted onto gelatin-coated slide glasses and dried for 24 h. The slides were rehydrated through 100% ethanol to distilled water, followed by dipping into staining solution. For Nissl staining, slides were placed in 0.1% cresyl violet solution for 5 min. For H&E staining, slides were placed in hematoxylin solution for 4 min followed by further staining with 0.25% eosin for 1 min. After quick rinsing with distilled water, the sections were dehydrated by ethanol at graded concentrations from 90 to 100%, followed by dipping into xylene. Finally, the slides were mounted with permanent medium. Brain images were observed and captured by microscope (SteREO, Discovery V8, Zeiss) connected with a CCD camera (AxioCam MRc, Zeiss).

AraC and Tamoxifen Treatment—P5 mice were anesthetized by hypothermia and placed on an inverted illuminating platform. Three microliters of 5% AraC in saline with 0.01% fast green dye were infused into the lateral ventricle by a Hamilton syringe. At P9 or P25, brain sections were prepared as described for the nano-bead tracing method. The sections were then immunostained as described under "Immunohistochemistry" or were Nissl-stained as described above. Images were obtained by confocal microscopy (LSM 710; Zeiss) or light microscope (SteREO, Discovery V8, Zeiss). Tamoxifen was administered by subcutaneous injection between the front shoulder blades two

times at P0 and P1 (0.2 mg/pup) into $Wrp^{\text{flox/flox}}$:N4CreER$^-$ mice and $Wrp^{\text{flox/flox}}$:N4CreER$^+$ mice.

Statistical Analyses—Student's t test (SPSS 12.0) was used for the analysis of a difference between two groups. All values were expressed as mean $\pm$ S.E., and results were considered statistically significant if $p < 0.05$.

RESULTS

Wrp KO Mice Exhibit Perinatal-onset Hydrocephalus—Recently, we generated a *Wrp* (*Srgap3*) knock-out mouse model to analyze the role of WRP in neural development (25). In the initial characterization of these mice, we noted enlarged LVs (25). This phenotype became more severe following backcross to C57BL/6, a strain that is susceptible to hereditary hydrocephalus (30–33), so that by $n8$–10 homozygotes exhibited swollen brains typical of hydrocephalus with complete penetrance (Fig. 1*A*). Intra-cranial magnetic resonance imaging (Fig. 1*B*) and surface rendering of the ventricular space (Fig. 1*C*) showed grossly enlarged LVs in the *Wrp* KO mice compared with WT littermates. Morphological studies with developing brains showed that this hydrocephalus did not initiate during embryogenesis but instead developed after birth (Fig. 1*D*). The LV size of *Wrp* KO mice was normal until postnatal day 9 (P9), and by P12 the KO brains ($n = 3$ for WT; $n = 4$ for KO) began to display enlarged LVs ($t = 4.29$, $df = 5$, $p < 0.01$) that were more severe at P40 ($n = 3$ for WT; $n = 4$ for KO) ($t = 14.87$, $df = 5$, $p < 0.0001$) (Fig. 1*E*). Ependymal cilia appeared normal in P12 KO mice (data not shown), suggesting the hydrocephaly was not due to ciliary defects. To determine whether the hydrocephalus is communicating or noncommunicating, Evans blue dye was injected into the LV of P40 mice. Surface viewing showed that the stain reached the spinal cord of WT mice, whereas no stain was found in the spinal cord of KO mouse (*blue arrows* in Fig. 1*F*). Serial coronal sectioning then showed the stain in LVs and third ventricle but excluded from the cerebral aqueduct (*red arrows* in Fig. 1*F*), indicating a blockage of the aqueduct leading to hydrocephalus. These data indicate that the hydrocephalus in the *Wrp* KO mice initiates at an early postnatal stage and ultimately results in obstructive hydrocephalus.

WRP Is Highly Expressed in the Ventricular Stem Cell Niche—To investigate the etiology of the hydrocephalus in *Wrp* KO mice, we first carried out *in situ* hybridization histochemistry and immunohistochemistry (IHC) to determine the relative expression pattern of *Wrp* mRNA and protein, respectively. *In situ* hybridization histochemistry with horizontal brain sections showed high levels of *Wrp* mRNA expression in LVs, in addition to the OB, hippocampus, and cerebellum throughout the postnatal periods (Fig. 2*A*). To confirm these data, IHC was performed using WT P40 sagittal brain sections. This clearly showed that WRP protein is highly expressed in the RMS and the SVZ (Fig. 2*B*). We note that lower levels of WRP are expressed in most other brain regions in addition to the RMS and SVZ (11). The pattern of WRP immunoreactivity overlapped that of BrdU, which was injected 4 days before sacrifice to label actively dividing cells within the SVZ, suggesting WRP is expressed in newborn progenitor cells originating from the SVZ. For a more detailed examination of individual cells, we
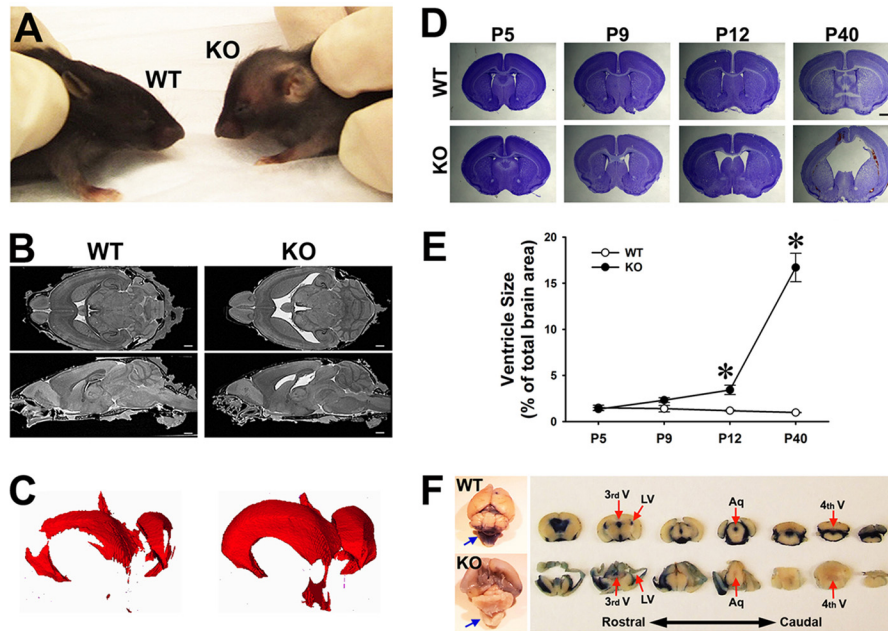
FIGURE 1. **Wrp KO mice exhibit perinatal-onset hydrocephalus.** *A,* P40 *Wrp* KO mouse displays dome-shaped head. *B,* intracranial magnetic resonance images using P77 *Wrp* KO mice and their WT littermates. Horizontal and sagittal views demonstrate enlarged ventricles in *Wrp* KO mice. *Scale bar,* 1 mm. *C,* representative surface renderings of the ventricular system from WT (*left*) and *Wrp* KO (*right*) mice generated from magnetic resonance imaging datasets. *D,* Nissl staining with developing postnatal brains from WT and KO. Coronal sections of P5, P9, P12, and P40 show a gradual increase of LV size in KO mice. *Scale bar,* 2 mm. *E,* quantification of LV area reveals that *Wrp* KO are normal at P5 and slightly enlarged at P9 (statistically insignificant). By P12, however, the LV size of KO is significantly increased compared with that of WT. *, $p < 0.01$. *F,* CSF circulating assay with P40 WT and *Wrp* KO mice. Evans blue dye infused into the LV is visible in the spinal cord of WT mice, whereas no stain is detected in that of KO mice (*blue arrows, left panel*). Serial sections show that Evans blue dye stains the entire ventricular cavities from LV level to 4th ventricle (*red arrows*) in WT mice. However, in KO mice, the dye is absent from the aqueduct. *3rd V*, third ventricle; *LV*, lateral ventricle; *Aq*, aqueduct; *4th V*, fourth ventricle.

performed co-IHC with WRP and DCX. Confocal Z-stack imaging showed that WRP is expressed within a subpopulation of DCX-positive cells within the RMS (Fig. 2*C*) and SVZ (Fig. 2*D*), in addition to ependymal cells (Fig. 2*D*). Collectively, these data suggest the possibility that like other members of the srGAP family, WRP may regulate the migration of newborn cells from the ventricular niche. Abnormalities in this migration might be related to the enlarged ventricles and development of hydrocephaly in the *Wrp* null animals.

Genetic Ablation of Wrp in the Ventricular Niche Leads to the Hydrocephalic Phenotype—If the main initiating factor of hydrocephalus in *Wrp* KO mice arises from abnormalities in the ventricular niche, specific deletion of *Wrp* in the niche area should lead to phenotypes that overlap those observed in the *Wrp* KO mice. To test this hypothesis, *Wrp*^{flox/flox} mice (25) were bred with Nestin-Cre-ER (N4CreER) transgenic mice (26). This approach has the advantage that the deletion of conditional alleles is restricted to Nestin-positive cells. Yet unlike germ line deletion, it is mosaic and does not occur with 100% efficiency (26). Tamoxifen was injected at P0 and P1 to delete *Wrp* expression in neuroprogenitors at an early postnatal stage. At this time point, tamoxifen treatment has been shown to result in recombination in neuroprogenitors surrounding the LV wall, as well as sparse neuroprogenitors within the cerebral cortex that are undergoing terminal differentiation (26). All *Wrp*^{flox/flox}:N4CreER[−] mice (10 total) were normal (Fig. 3, *A–D*). In contrast, we found markedly enlarged LVs in three of seven *Wrp*^{flox/flox}:N4CreER⁺ mice (Fig. 3*H*), consistent with the mosaic activation of Cre activity in neural progenitors after tamoxifen treatment. A mild phenotypic effect in *Wrp*^{flox/flox}:

N4CreER⁺ mice may be due to a restricted portion of progenitor cells undergoing *Wrp* deletion when compared with *Wrp* KO mice. IHC analysis of the affected *Wrp*^{flox/flox}:N4CreER⁺ mice showed the presence of DCX-positive neuroblasts located along the CC area (Fig. 3*I, arrows*). Moreover, the Nestin signals were also increased in the CC, a subpopulation of which expressed DCX (Fig. 3, *I–K, insets*). In contrast, very few neuroblasts and Nestin-positive cells were found in CC area of *Wrp*^{flox/flox}:N4CreER[−] mice (Fig. 3, *B–D*). Moreover, a large portion of DCX-positive cells were abnormally localized within the ventral region of the LVs (Fig. 3*D, arrowheads*), leading to the formation of astroglial cell masses that are positive for Nestin and aquaporin-1 (AQP1), resulting in tissue disruptions (Fig. 3, *L–N*). AQP1 has previously been implicated as a marker of neoplastic cell masses (34–37). These genetic data suggest that *Wrp* deficiency within the ventricular niche can mimic the hydrocephalus observed in the *Wrp* null mice, although it is possible progenitors within the cerebral cortex also contribute to the phenotype. Nonetheless, the data support a relationship between abnormal progenitor cells and onset of hydrocephalus.

Normal Progenitor Cell Organization Is Disrupted in Wrp KO Mice—Because WRP is highly expressed in the ventricular stem cell niche and because abnormal localization of progenitor cells were observed in *Wrp*^{flox/flox}:N4CreER⁺ mice, we suspected a prominent abnormal progenitor migration out of ventricular niche by complete loss of *Wrp*. Thus, we further investigated the distribution and migration of progenitor neuroblasts in the SVZ and RMS of *Wrp* KO mice. Immunostaining with DCX revealed that a large portion of neuroblasts were stacked in the entry point of RMS (Fig. 4, *A* and *B, yellow arrowhead*). In addi-
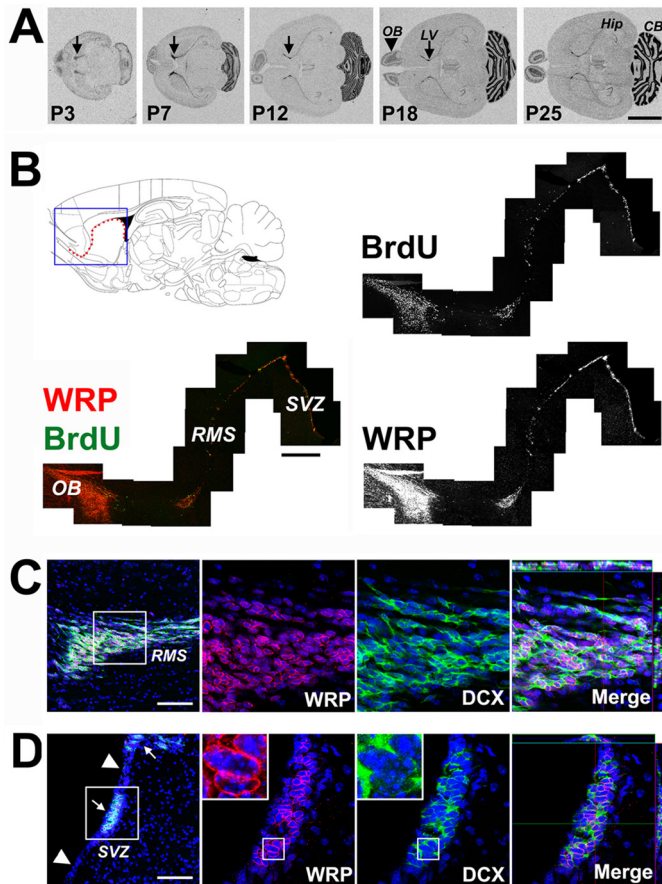
FIGURE 2. WRP is expressed in the ventricular stem cell niche. *A, in situ* hybridization histochemistry detecting *Wrp* within developing brains. *Wrp* mRNA is highly expressed in the ventricular zone (*arrows*) as well as olfactory bulb (*arrowhead*), hippocampus, and cerebellum throughout the postnatal development. Note the dense labeling in the LVs at perinatal stage (P3 to P12). *OB,* olfactory bulb; *Hip,* hippocampus; *CB,* cerebellum. *Scale bar,* 5 mm. *B,* sagittal brain map showing the SVZ lining and RMS stack (*red dots*). Double immunostaining demonstrates that the expression pattern of WRP is very similar to BrdU signals in the ventricular niche area. *RMS,* rostral migratory stream; *SVZ,* subventricular zone. *Scale bar,* 500 µm. *C,* double labeling for WRP and DCX in RMS reveals that WRP protein is highly expressed in RMS where DCX-positive neuroblasts are located. Z-stack imaging (*right panel*) shows WRP expression in a subpopulation of DCX-positive cells within the RMS. *Scale bar,* 100 µm. *D,* immunostaining shows strong WRP immunoreactivity in the SVZ (*arrows*) but not in the DCX-negative cell population (*arrowheads*). Z-stack imaging (*right panel*) shows WRP expression in a subpopulation of DCX-positive cells in SVZ. *Scale bars,* 100 µm.

FIGURE 3. Knock-out of *Wrp* in the ventricular niche induces the hydrocephalic phenotype. *A* and *H,* Nissl staining of sagittal sections from P40 *Wrp*$^{flox/flox}$:N4CreER$^-$ and *Wrp*$^{flox/flox}$:N4CreER$^+$ mice. *Red box* indicates dorsal part, and *blue box* indicates ventral part of the LVs. *A,* control *Wrp*$^{flox/flox}$:N4CreER$^-$ mice display a normal dorsal LV morphology. *Scale bar,* 1 mm. *H, Wrp*$^{flox/flox}$:N4CreER$^+$ mice show an enlarged LV and an abnormal cell mass within the ventral region of the LV (*green arrow*). *B–D,* immunohistochemical analysis shows DCX-positive neuroblasts, and Nestin-positive cells are predominantly localized in the SVZ and RMS of *Wrp*$^{flox/flox}$:N4CreER$^-$ mice. Dense Nestin signals in the ependyma and moderate signals in SVZ are observed in *Wrp*$^{flox/flox}$:N4CreER$^-$ mice, and evenly distributed DCX signals are detected in RMS and SVZ. *Cpu,* caudate putamen. *Scale bar,* 100 µm. *E–G,* control *Wrp*$^{flox/flox}$:N4CreER$^-$ displays normal shape of ventral region of LV with AQP1 signals only in the choroid plexus. *cp,* choroid plexus. *I,* in *Wrp*$^{flox/flox}$:N4CreER$^+$, however, a large portion of neuroblasts are observed along the CC area (*white arrows*) and ventral part of the LV (*arrowhead*). *J,* strong Nestin immunoreactivity is also observed in the CC and ventral LV area aside from the ependyma and the SVZ in *Wrp*$^{flox/flox}$:N4CreER$^+$ mice. *K,* both DCX and Nestin signals are evenly distributed in ependyma, SVZ, and ventral LV. *Arrowheads* indicate the expression of DCX and Nestin in the abnormal cell mass located in ventral LV. A subpopulation of Nestin-positive cells in CC area also express DCX (*insets*). *Scale bar,* 20 µm. *Asterisks* indicate enlarged LV. *L–N, Wrp*$^{flox/flox}$:N4CreER$^+$ shows abnormal cell mass in which partial Nestin- and AQP1-positive signals are detected. Note the partial tissue damage around the cell mass (*yellow arrows*). *Scale bar,* 200 µm.

tion, neuroblasts were mislocalized and scattered along the CC above the dorsal plate of the LV (Fig. 4*B, white arrows*). This subpopulation of KO neuroblasts had lost their normal migrational orientation toward the RMS and olfactory bulb. High magnification view of the RMS showed that DCX-positive cells in KO brains were dispersed and misoriented in direction when compared with the well organized neuroblasts in WT mice (Fig. 4, *panels a* and *b*). Directional coherence revealed that the angle variations of the DCX-positive KO ($n = 4$) cell processes were significantly higher than that of WT ($n = 4$) ($t = 11.61, df = 6,$ $p < 0.0001$) (Fig. 4, *C* and *D*), consistent with a highly aberrant progenitor cell migration. We next determined the temporal relationship between the progenitor cell mis-migration and the initiation of hydrocephalus, because there is a possibility that the aberrant progenitor cell distribution could be caused by tissue damage related to hydrocephaly. Thus, we analyzed early
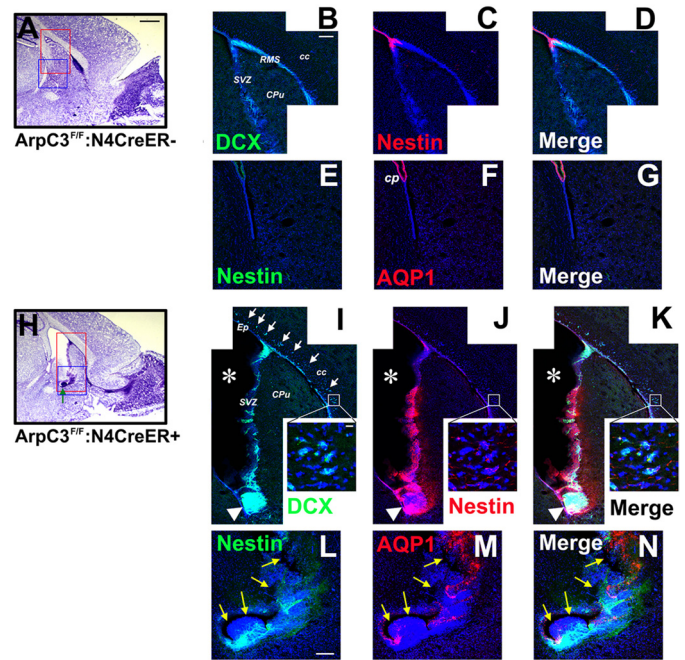
postnatal KO brains, before the onset of aqueductal occlusion and enlargement of LVs (see below). DCX IHC through the rostral and ventricular CC of P9 coronal brain sections exhibited an increased incidence of neuroblasts in the CC of KO mice (Fig. 4, *E–H*). Quantification revealed a significant increase of DCX-positive neuroblasts in the rostral CC ($t = 9.69, df = 4,$ $p < 0.0001$) and the ventricular CC ($t = 5.07, df = 4, p < 0.01$) when compared with WT ($n = 3$ for each group) (Fig. 4, *I* and *J*). These data suggest that *Wrp* deletion in progenitor cells gives rise to abnormal localization of progenitor cells in the CC area before the ventricular dilation.

Abnormal Progenitor Migration from the Ventricular Wall into the Corpus Callosum in Wrp KO Mice—Because the localization of DCX-positive cells was abnormally found in the CC region in the *Wrp* null mice, the possibility of a migration defect was tested by two independent lineage tracing methods in the *Wrp* null animals. First, fluorescent nano-beads (40 nm diame-
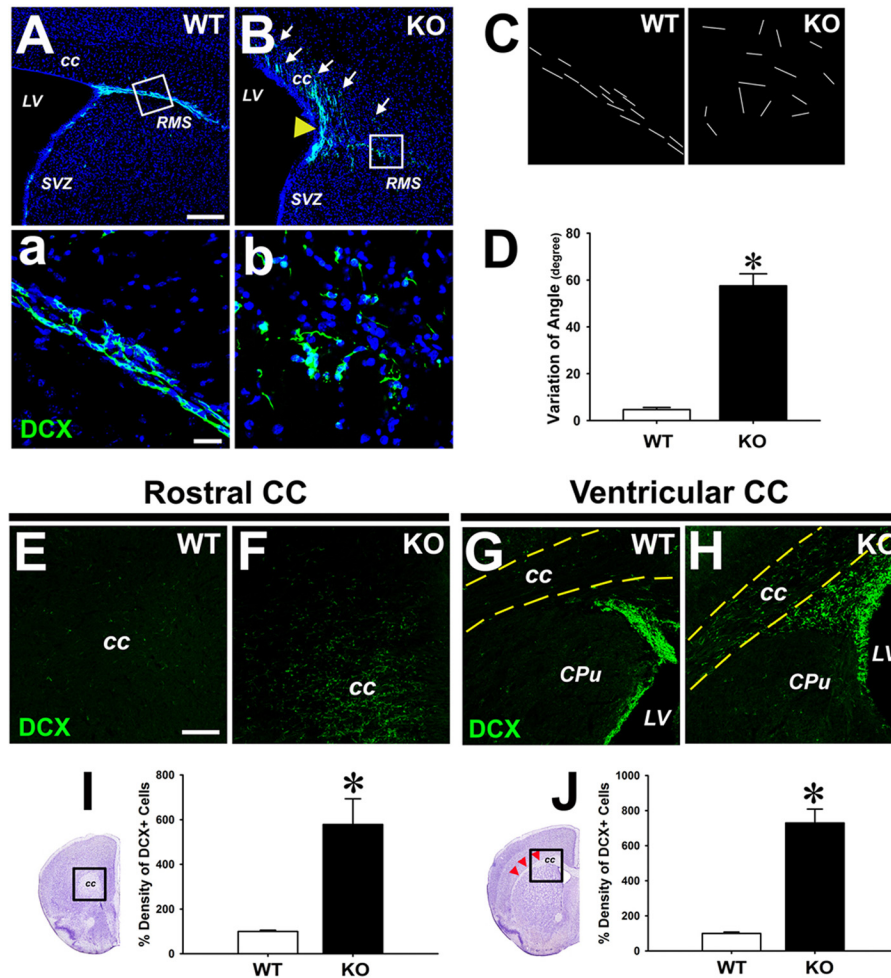
FIGURE 4. **Aberrant migration of progenitor cells following *Wrp* deletion.** *A–D*, mis-localization of DCX-positive neuroblasts of the ventricular zone and the RMS in P40 *Wrp* KO mice. *A*, WT sagittal section shows specific and normal localization of DCX-positive cells in the SVZ and RMS. *Scale bar*, 200 μm. *Panel a*, angles of each neuroblasts are homogeneously organized through the RMS track. *Scale bar*, 50 μm. *B*, *Wrp* KO mice show mis-localized neuroblasts in the CC above the dorsal plate of the LV (*arrows*) and stacked neuroblasts at the entry point of RMS (*yellow arrowhead*). *Panel b*, high magnification view of the RMS shows dispersed and misoriented neuroblasts in KO RMS when compared with WT. *C*, representative cell angles (matching to *panels a* and *b*) showing the orientation of each neuroblast based on DCX staining in the RMS for WT (*left*) and KO (*right*). *D*, quantification reveals that the angle variation (standard deviation) of the KO cell orientation in the RMS is significantly higher than that of WT. *E–J*, mis-localization of neuroblasts in P9 *Wrp* KO mice. Coronal brain sections of WT mice show very little evidence of DCX-positive cells in the rostral (*E*) or ventricular CC (*G*) regions. In contrast, *Wrp* KO mice exhibit extensive DCX-positive neuroblasts in the rostral (*F*) and ventricular CC (between *yellow dashed lines*) *H*, representative brain slices (*left side* of graphs) represent the areas (*boxed region*) used for measuring DCX-positive cells. Quantification reveals a significant increase of DCX-positive cells in the KO CC both in the rostral and ventricular CC (*red arrowheads*) when compared with WT (*I* and *J*). *Scale bar*, 200 μm. *EP*, ependyma; *CPu*, caudate putamen; *CC*, corpus callosum. *, $p < 0.01$.

ter), which can be used to trace migrating neuroblasts (38), were used to observe the migration of cells from the ventricular wall. For this experiment, we infused the fluorescent nanobeads into the LV of WT and KO mice at P5 and analyzed their localization at P12. In WT animals, most of the beads were detected along the LV wall and the entry point (*yellow arrow*) to the RMS (Fig. 5*A*). In contrast, a large portion of the beads was observed in a puncta-like manner in the *Wrp* KO CC (Fig. 5*B*). Densitometry plots (Fig. 5, *panels a* and *b*) clearly showed a random distribution of the beads in the CC area of KO mice (Fig. 5, *panel b*). Quantification of the bead density showed a marked increase of beads within the KO CC ($n = 3$ for each group) ($t = 41.05$, $df = 4$, $p < 0.0001$), whereas no difference was found in the ventricular wall (Fig. 5*C*), suggesting aberrant cell migration from the ventricular wall into the CC area in the perinatal KO mice. Significantly, the cell density of the KO CC areas that were used for the nano-bead tracing study was similar to that of WT, indicating healthy tissue (data not shown).

Viral lineage tracing was used to further verify the origin of the aberrant cells within the CC of *Wrp* KO animals. tdTomato-expressing lentivirus was infused into the LV of P3 brains, followed by lineage tracing of the infected cells within the dorsal plate of the ventricle at P12. WT infected cells were detected only in the ventricular wall (Fig. 5, *D* and *E*, *arrowheads*). However, the infected cells in KO mice were frequently observed in the CC. These cells also expressed Nestin (Fig. 5*F*, *arrows*), implying that the cells possess stem cell-like property. High magnification view of Z-stack images demonstrated co-localization of the tdTomato and the Nestin signals in a subpopulation of cells with an astrocyte-like morphology (Fig. 5*G*, *arrow*), suggesting the possibility that the mis-migrated cells developed into astrocytes in CC and led to abnormal astrogliosis. Importantly, infected cells were also observed in the olfactory bulb in both the WT and KO animals (Fig. 5, *H–K*), showing the infection-labeled neural progenitor cells. The cell densities in the CCs of the KO mouse samples used in this study were also
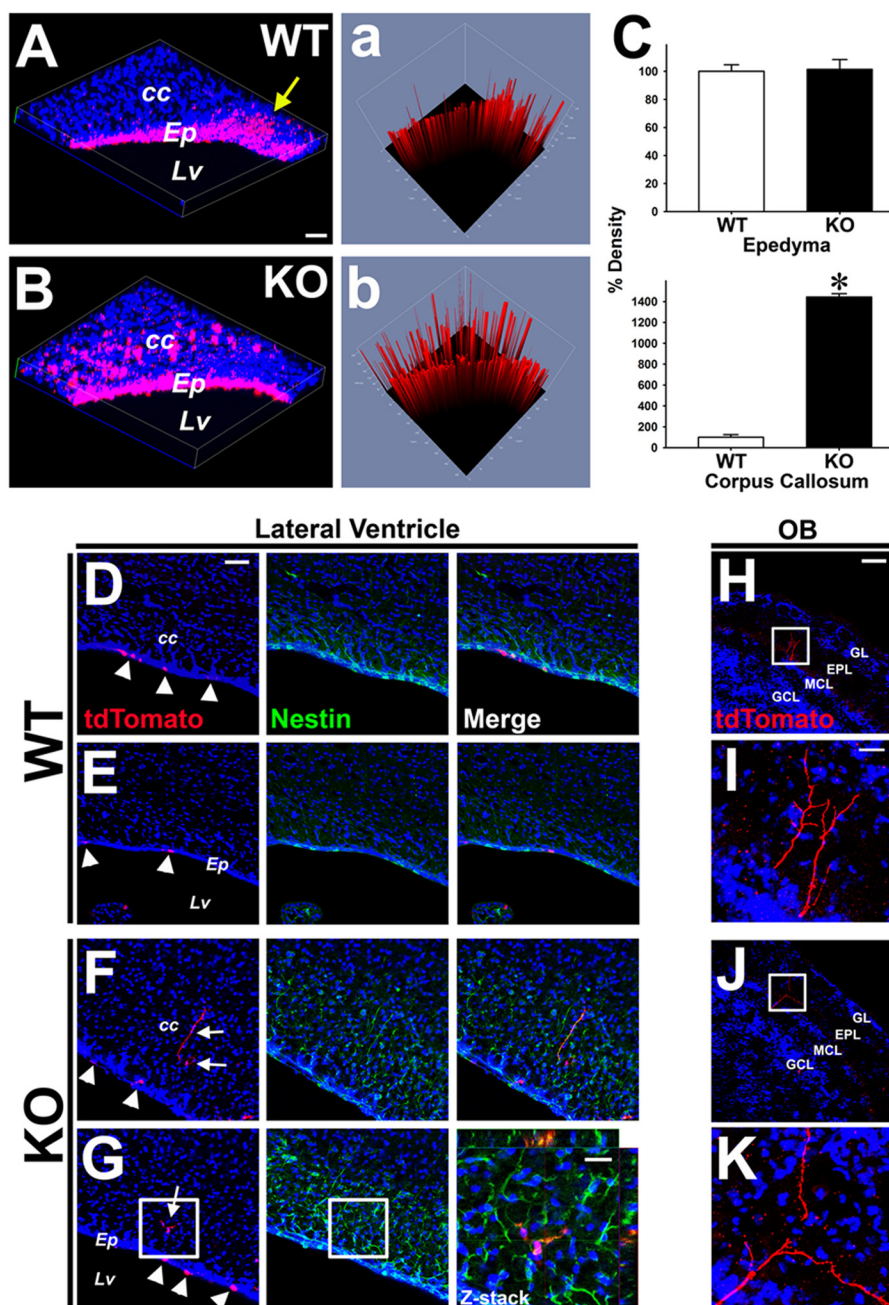
FIGURE 5. **Abnormal cell migration from the ventricular wall region into the corpus callosum in *Wrp* KO mice.** *A–C,* fluorescent nano-bead injection into the ventricles of P5 mice followed by tracing of the beads at P12. *A,* beads are observed in the WT LV wall and the entry point to the RMS (*yellow arrow*). *Ep,* ependyma. *Scale bar,* 50 μm. *B,* in KO mice, however, a large portion of the beads is detected in the CC as well as in the ependymal layer. *Panels a* and *b,* densitometry plots showing the distribution of the beads in the CC area of the WT and KO mice. *C,* quantification reveals identical bead density between WT and KO in the ependymal layer (*bottom*), yet a significant increase in beads in the CC of KO mice. *, $p < 0.0001$. *D–G,* representative images (two WT and two KO) of lineage tracing by lentiviral infection of the LV wall. *D* and *E,* infected cells (infection at P3) are detected only in the ventricular wall of WT (*arrowheads*) at P12. *Scale bar,* 50 μm. *F,* however, in the KO mice, the infected cells are observed in CC area (*white arrows*). Note that these cells express Nestin. *G,* subpopulation of the infected cells show astrocyte-like morphology (*white arrow*). High magnification Z-stack image view of the *boxed region* demonstrates co-localization of the tdTomato and the Nestin signals in the cells (*right panel*). *Scale bar,* 20 μm. *H* and *J,* tdTomato-positive cells are detected in olfactory bulb of WT and KO. *OB,* olfactory bulb; *GL,* glomerular layer; *EPL,* external plexiform layer; *MCL,* mitral cell layer; *GCL,* granule cell layer. *Scale bar,* 100 μm. *I* and *K,* high magnification view shows neuronal morphology of the tdTomato-positive cells in olfactory bulb. *Scale bar,* 20 μm.

normal (data not shown). Together, these independent methods of cell lineage tracing show the progenitor cells of the niche area in perinatal *Wrp* KO mice abnormally migrate into the CC, likely leading to the initiation of the astrogliosis.

Astrogliosis in Corpus Callosum Precedes the Occlusion of the Ventricular System—Interestingly, the first evidence of tissue disruption in the *Wrp* KO mice was manifested by periventricu-

lar cystic cavities that formed in the perinatal CC adjacent to the CA1 part of hippocampus (Fig. 6*B, asterisk*). IHC with P9 KO mice showed strong GFAP signals around the cystic cavity, suggesting specific astrogliosis in the CC area. Surprisingly, CSF circulation assay revealed that the aqueducts of KO mice were open during this period (*red arrows*), and the Evans blue dye was clearly detectable in the lesions of the CC located in the
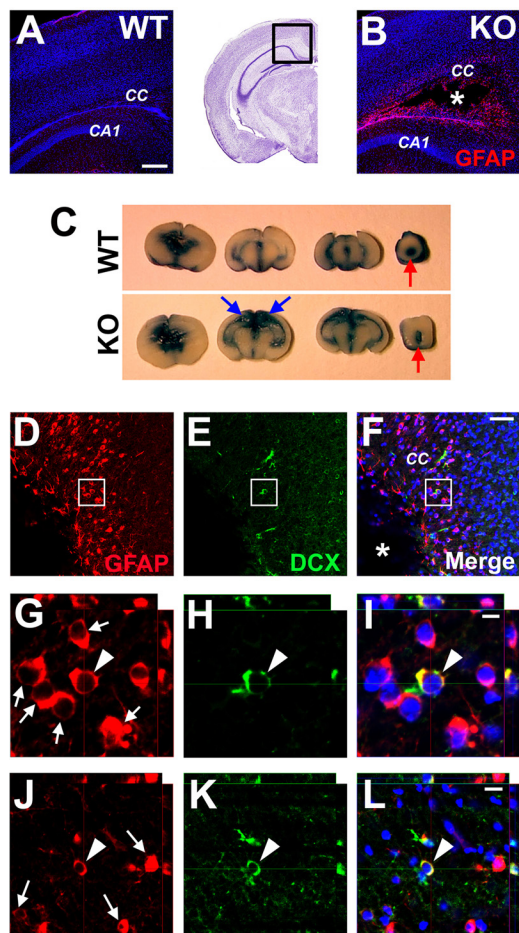
FIGURE 6. **Corpus callosum damage precedes the blockage of the ventricular cavity.** *A–C*, brain image on the *top panel* represents the hippocampal level of corpus callosum (*box*) that is used for immunostaining. *A*, at P9 WT shows no tissue disruption and expresses little GFAP in the CC area. *Scale bar*, 200 μm. *B*, P9 KO exhibits ectopic cystic cavity (*asterisk mark*) in the CC above the hippocampus with a high expression of GFAP. *C*, in this period (P9), both WT and KO display Evans blue stain in aqueduct (*red arrows*), indicating an open aqueduct. Note the blue stains in the ectopic cavities above the KO hippocampi (*blue arrows*). *D–I*, GFAP- and DCX-double positive cells around the cystic cavity. High magnification view of P9 KO brain shows an elevated level of GFAP-positive astrocytes (*D*) and DCX-positive neuroblasts (*E*). *F*, double-positive cells are observed in subcystic cavity area. *Asterisk*, cystic cavity; *scale bar*, 100 μm. Higher magnified Z-stack images of the region (*white boxes*) clearly show individual GFAP-positive cells (*white arrows*) (*G*) and DCX-positive cell (*H*). *I*, subpopulation of GFAP-positive cells also express DCX (*white arrowhead*). *Scale bar*, 10 μm. *J–L*, Z-stack images of rostral CC demonstrate GFAP-positive astrocytes (*arrows*) (*J*) and DCX (*K*) in P9 KO mice. Merged image demonstrates subpopulation of GFAP-positive cells express DCX (*arrowhead*) (*L*). *Scale bars*, 20 μm.

hippocampal plane (*blue arrows*) (Fig. 6*C*). This phenotype was confirmed by consecutive studies of Evans blue tracing with six KO mice (data not shown). These data demonstrate that at the onset of hydrocephalus in the *Wrp* KO mice, abnormal astrogliosis is associated with cystic lesions of the CC region and that the astrogliosis precedes the blockage of the aqueduct. To understand the relationship between the astrogliosis and the mismigrated progenitor cells, we investigated the identity of progenitor cells around the cystic cavity. We observed that DCX-positive neuroblasts and GFAP-positive astrocytes resided around the cavity area (Fig. 6, *D–F*). High magnification Z-stack images showed that a subpopulation of DCX-positive cells expressed GFAP in the subcavity area (Fig. 6, *G–I*), sug-
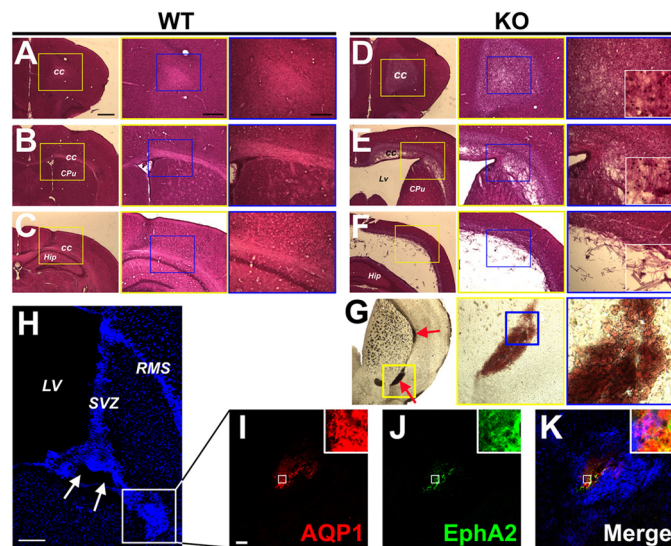

FIGURE 7. **Astrogliosis in the corpus callosum and the ventral LV of the *Wrp* KO mice.** *A–F*, H&E staining shows astrogliosis in CC area of P40 *Wrp* KO mice. Normal morphology in rostral (*A*), ventricular zone (*B*), and hippocampal (*C*) region of the CC in WT mice. *D–F*, CC areas in *Wrp* KO mice are damaged, whereas the cortex, caudate putamen (*E*), and the hippocampus (*F*) appear normal. High magnification views show astrogliosis throughout the CC area (*right panels* of *D* and *E*). Note that axonal debris is released from the CC region into the ventricles (*right panel* of *F*). *cc,* corpus callosum; *CPu,* caudate putamen. *Scale bars,* 1 mm (*left panel*); 500 μm (*middle panel*); 200 μm (*right panel*). *G,* focal hemorrhages in the corpus callosum of *Wrp* KO mice. Sequential high magnification views (*yellow* and *blue boxes*) with perfused (nonstained) P40 *Wrp* KO brain sections clearly display bleeding in the deep ventrolateral part of the CC (*red arrow*). *H–K,* astroglial cell mass in the ventral part of LV in *Wrp* KO mice. *H*, DAPI staining with sagittal section from KO brain reveals the abnormal cell mass (*white box*) in the ventral part of LV with partial tissue damage (*arrows*). *Scale bar,* 500 μm. Immunostaining shows that AQP1 (*I*) and EphA2 (*J*) are expressed in the central part of the abnormal cell mass. *K*, both signals partially merged with each other.

gesting that the neuroblasts in KO CC also possess astroglial identity. These double-positive cells were never observed in WT CC. This phenotype implies a possible transition of mismigrated neuroblasts into astrocytes, leading to the astrogliosis and the initiation of hydrocephaly. To further rule out the possibility that ventricular pressure-induced mechanical damage triggers the astrogliosis in the CC adjacent to the ventricles, we analyzed at P9 the very rostral CC that is distal to the ventricular area. IHC showed that a subpopulation of the GFAP-positive cells was also positive for DCX (Fig. 6, *J–L*). Together, these data demonstrate a unique developmental timeline for hydrocephalus development in which CC lesions associated with astrogliosis precede blockage of the cerebral aqueduct. Our data also suggest that cystic cavities in the KO mice may initiate the detachment of the CC from neighboring tissues during the early perinatal period, contributing to the enlarged LV space observed in these animals. Based on the lineage tracing experiments (Fig. 5), the likely source for the initiation of these lesions is from abnormal migration of progenitor cells out of the ventricular zone.

Progression of Astrogliosis in the Corpus Callosum of Wrp KO Mice—Hematoxylin and eosin (H&E) staining of WT (Fig. 7, *A–C*) and KO brains (Fig. 7, *D–F*) revealed a massive disruption of tissue in P40 *Wrp* KO brains, predominantly within the CC of rostral (Fig. 7*D*), ventricular (Fig. 7*E*), and hippocampal areas (Fig. 7*F*). Adjacent tissues, however, such as the hippocampus,
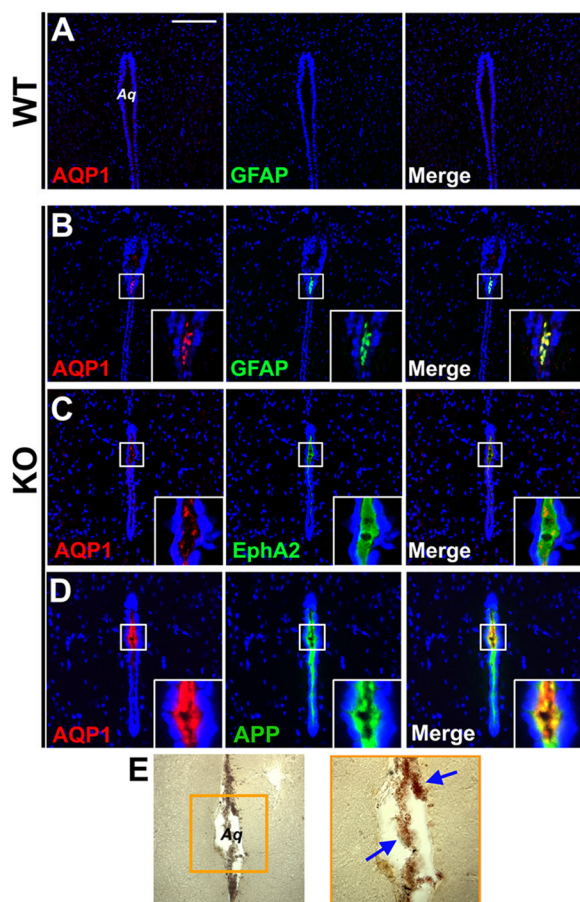
FIGURE 8. **Aqueduct of *Wrp* KO mouse (P40) is blocked by astrogliosis, axonal debris, and hemorrhage.** *A,* WT shows no AQP1/GFAP-positive debris inside the aqueduct. *Aq,* aqueduct. *Scale bar,* 100 μm. *B,* KO mice show aqueductal obstructions that are positive for AQP1/GFAP. *C,* KO mice show aqueductal obstructions that are positive for AQP1/EphA2. The substances inside of aqueduct are nucleus-free debris. *D,* KO mice also show APP-positive nucleus-free axonal debris inside of the aqueduct. *E,* hemorrhages are observed in the KO aqueduct. High magnification view (*orange box*) shows the existence of the hemorrhage inside of the aqueduct (*blue arrows*).

cortex, or caudate putamen appeared to be normal (Fig. 7, *E* and *F*). High magnification views showed evidence that axonal debris released from the CC region enters the ventricles (Fig. 7*F*). Moreover, focal hemorrhages were observed along the KO CC area (Fig. 7*G*), giving further evidence of focal astrogliosis-associated damages in the CC of *Wrp* KO mice. Taken together, these data suggest that in *Wrp* KO mice initial lesions within the CC region ultimately result in tissue damage and release of debris into the ventricles that precede the aqueductal occlusion. Additionally, abnormal cell masses were also observed in the ventral part of the LVs in the KO mice (Fig. 7*H*) that were positive for AQP1 and ephrin type-A receptor 2 (EphA2), another neoplastic astroglial marker (Fig. 7, *I–K*) (39, 40).

Aqueduct of Wrp KO Mice Is Blocked by Astrogliosis and Axonal Debris—Might the cystic cavities be linked to the ensuing occlusion of the aqueduct? To assess this possibility, IHC for AQP1, GFAP, EphA2, and APP in WT and KO brain sections in the aqueductal region was performed. In WT animals, no immunopositive signals of astrogliosis debris were found in aqueductal serial sections (Fig. 8*A*). In contrast, AQP1, GFAP, and EphA2 signals were detected inside the rostral part of the

aqueduct in P40 KO mice (Fig. 8, *B* and *C*). In addition, APP, a marker of axonal debris (41), was also observed inside of KO aqueducts (Fig. 8*D*). Furthermore, the focal hemorrhage clots in the aqueduct were readily detectable (Fig. 8*E*). Because our observations have shown the axonal debris and the hemorrhages within the KO CC, the aqueductal occlusion is likely to have originated from the damaged CC area. These data strongly suggest that the aqueductal obstructions are induced by the astrogliosis and axonal debris that are caused by the initial development of cystic CC lesions.

Hydrocephalus of Wrp KO Mice Is Reduced by AraC Treatment at Perinatal Period—Because abnormal migration of progenitor cells in *Wrp* KO mice appear to initiate enlargement of the ventricle, we hypothesized that the inhibition of cell proliferation in the ventricular zone may alleviate ventricle enlargement of *Wrp* KO mice. To evaluate this hypothesis, we treated knock-out mice with the mitotic inhibitor AraC at the critical perinatal period (P5–P9). We infused 3 μl of 5% AraC ($n = 4$) *versus* saline ($n = 4$) into the lateral ventricle of P5 *Wrp* KO mice and measured the ventricle size at P25 (Fig. 9, *A–C*). We found the ventricle sizes of AraC-treated brains were significantly smaller than those of the saline-treated control group ($t = 2.94$, $df = 6$, $p < 0.05$) (Fig. 9*C*), suggesting that the reduction of progenitor cell proliferation during the perinatal period may relieve the hydrocephalic phenotype in *Wrp* KO mice. The reduction of progenitor cell proliferation was confirmed following the infusion of AraC into the lateral ventricle of WT P5 brains. This treatment resulted in a reduction of Ki-67-positive proliferating cells in the Nestin-positive progenitor cell population within the entry point of RMS at P9 (Fig. 9, *D* and *E*).

DISCUSSION

The *Wrp* postnatal hydrocephalic mouse model leads us to propose the following mechanism for the initiation and progression of hydrocephalus. Importantly, this pathology begins with the aberrant migration of cells from the ventricular zone caused by *Wrp* deficiency. This abnormal migration is analogous to that previously described for the related srGAP1- and srGAP2-deficient progenitors (7, 9, 10), but with a distinct pathological outcome. In the case of *Wrp* deficiency, these ectopic cells appear to be linked with the formation of focal cystic cavities in the CC area, leading to astrogliosis and lesions along the LVs. Debris originating from the disrupted CC subsequently obstructs the aqueduct, accelerating the gross enlargement of the lateral ventricles.

Sequence of Hydrocephalus Development in Wrp KO Mice—According to the classical theory for the etiology of hydrocephalus, the blockage of ventricular cavities initiates obstructive hydrocephalus development, leading to enlargement of ventricles and mechanical damage to tissues adjacent to the ventricles. Surprisingly, however, the initial processes or factors that give rise to aqueductal obstruction and hemorrhage are poorly defined. In *Wrp* KO mice, specific lesions within the CC derived from the ventricular zone preceded the ventricular obstruction, suggesting an alternative model in which focal periventricular damage gives rise to aqueductal obstruction followed by secondary tissue damage caused by increased ventricular pressure.
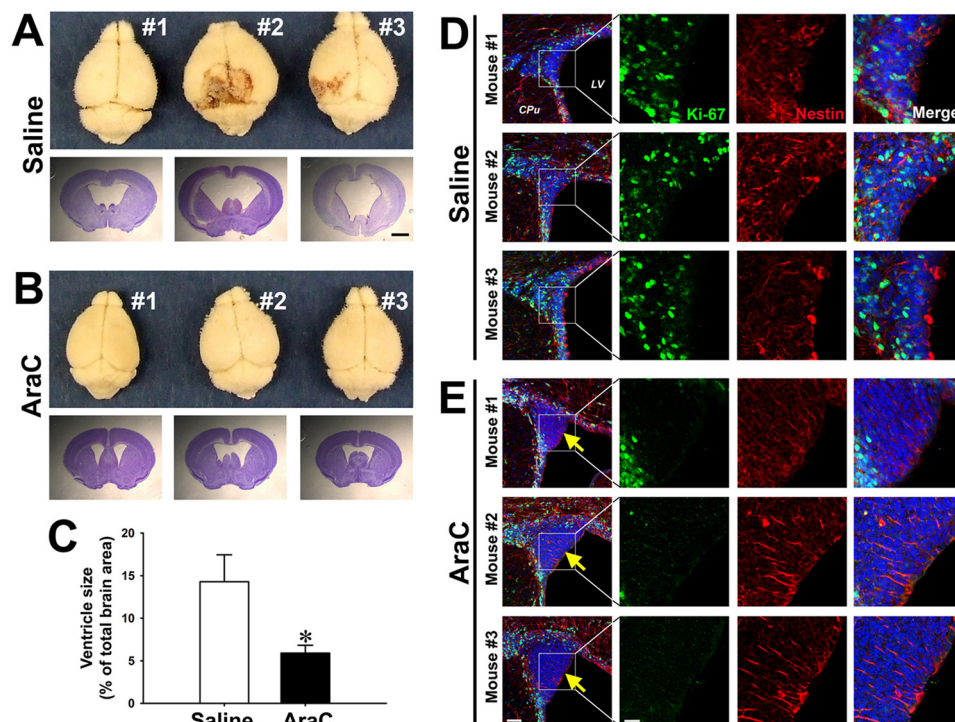
FIGURE 9. **AraC treatment relieves ventricle enlargement in *Wrp* KO mice.** *A*, KO mice treated with saline at P5 exhibit increased brain size (*upper panel*) with profoundly enlarged ventricles at P25 (*lower panel*). *Scale bar,* 2 mm. *B,* AraC-treated (at P5) KO brains are smaller than saline-treated KO brains (*upper panel*). Nissl staining shows reduced ventricle size compared with control KO brains (*lower panel*). *C, graph* of ventricle size reveals that AraC-treated KO ventricular size is significantly smaller than that of saline-treated KO controls. *, $p < 0.01$. *D,* saline-treated (at P5) control mice show evenly distributed expressions of Ki-67 in Nestin-positive ventricular niche at P9. High magnification views (*right panels*) show nuclear localization of Ki-67 combined with cytoplasmic Nestin signals. *E,* Ki-67-positive proliferating cells in entry point of RMS (*yellow arrows*) are reduced by the treatment of AraC. *Scale bars,* 50 μm (*1st column*), 20 μm (*2nd column*).
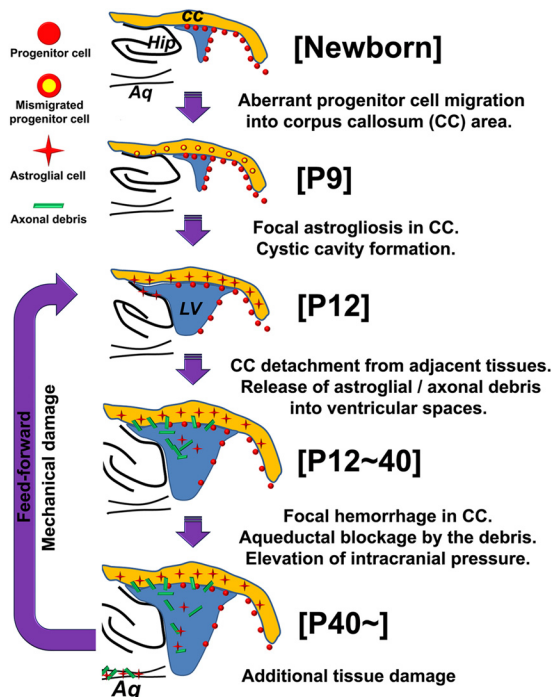

FIGURE 10. **Schematic showing the sequence of events leading to hydrocephalus development in the *Wrp* KO mice.** Developmental sequence of hydrocephalus is shown from *top to bottom*. Relative age of mice corresponding to each event leading to hydrocephalus is shown in *brackets*. *Aq,* aqueduct.

In this case, hydrocephalus can be considered a feed-forward-like pathology of contributing events initiated by the altered migration of ventricularly derived cells (Fig. 10).

Risk of Hydrocephalus during the Early Postnatal Period—The perinatal stage is a high risk period for hydrocephalus with the majority of patients diagnosed as infants. *Wrp* KO mice also showed perinatal-onset hydrocephalic symptoms with aberrant astrogliosis and focal damage within the CC region. Importantly, neural progenitor cell production peaks during this perinatal period. In rodents, the amount of progenitor cell production in the ventricular niche of P12 mice is 40-fold higher than that of P49 mice (24). Thus, it is reasonable to expect that this may represent a high risk period for the abnormal development of progenitor cells, such as migration defects or abnormal proliferation, leading to associated brain pathologies. In view of our data, the stem cell production or maintenance defects in the ventricular niche reported in Musashi knock-out mice, which also showed severe perinatal hydrocephalus with subventricular tissue disruptions (42), supports an unsuspected link between the stem cell niche and hydrocephalus. In agreement with this notion, fibroblast growth factor 2 (FGF-2) infusion into the LV induced overproduction of SVZ progenitor cells (43), and similar treatment of FGF-2 into the embryonic ventricle also caused hydrocephalic symptoms (44). Moreover, the expression of a constitutive active form of epidermal growth factor receptor in the frontal lobe, including the LV, is associated with hydrocephalus, abnormal cell masses, and hemorrhages (45). It is well known that EGF treatment gives rise to a strong expansion of neural progenitor cells as well as migration defects (46). It is also proposed that the multipotent SVZ neural progenitors are a source of transformed cells that give rise to gliomas (20–23). These reports together sup-

port the likelihood that the development of hydrocephalus is intimately associated with astrogliosis (and possibly subtypes of gliomas) that is caused by abnormalities of the ventricular stem cell niche and that the infant period is exposed to a high risk of the hydrocephalic development from cells within this region. If identified early enough, it is possible that chemotherapeutic approaches, analogous to AraC infusion, may be useful in reducing the development of progenitor cell-based disorders.

Astrogliosis in the CC of the Human Hydrocephalic Brain—Periventricular white matter, including the CC, is the primary target of hydrocephalus even in idiopathic normal pressure hydrocephalus (47, 48). Human hydrocephalic patients commonly show CC damage, including astrogliosis with axonal degeneration (49, 50), which is modeled in the *Wrp* KO mice. Currently, the astrogliosis is usually understood as a reactive astrocytosis induced by pressure-mediated mechanical damages in subventricular areas. Contrary to the previously held belief, *Wrp* KO mice showed astrogliosis before aqueductal blockage or enlargement of LVs, suggesting novel factors that initiate the astrogliosis. Our analysis shows that the source of the astroglial cells in the CC area arises from abnormal cells that originated from the ventricular stem cell niche where WRP is highly expressed in the perinatal period.

In this study, we proposed a previously unsuspected concept for explaining an etiology and pathogenesis of hydrocephalus by use of the *Wrp* KO mouse model. Our animal model resembles the phenotypes shown in infant hydrocephalus and allowed for the detailed analysis of the hydrocephalic development. This analysis suggests that investigations into possible abnormalities of the ventricular stem cell niche in human hydrocephalic patients are warranted.

REFERENCES

1. Beni-Adani, L., Biani, N., Ben-Sirah, L., and Constantini, S. (2006) The occurrence of obstructive vs. absorptive hydrocephalus in newborns and infants. Relevance to treatment choices. *Childs Nerv. Syst.* **22,** 1543–1563
2. Banizs, B., Pike, M. M., Millican, C. L., Ferguson, W. B., Komlosi, P., Sheetz, J., Bell, P. D., Schwiebert, E. M., and Yoder, B. K. (2005) Dysfunctional cilia lead to altered ependyma and choroid plexus function and result in the formation of hydrocephalus. *Development* **132,** 5329–5339
3. Davy, B. E., and Robinson, M. L. (2003) Congenital hydrocephalus in hy3 mice is caused by a frameshift mutation in *Hydin,* a large novel gene. *Hum. Mol. Genet.* **12,** 1163–1170
4. Ibañez-Tallon, I., Pagenstecher, A., Fliegauf, M., Olbrich, H., Kispert, A., Ketelsen, U. P., North, A., Heintz, N., and Omran, H. (2004) Dysfunction of axonemal dynein heavy chain Mdnah5 inhibits ependymal flow and reveals a novel mechanism for hydrocephalus formation. *Hum. Mol. Genet.* **13,** 2133–2141
5. Lindeman, G. J., Dagnino, L., Gaubatz, S., Xu, Y., Bronson, R. T., Warren, H. B., and Livingston, D. M. (1998) A specific, nonproliferative role for E2F-5 in choroid plexus function revealed by gene targeting. *Genes Dev.* **12,** 1092–1098
6. Tissir, F., Qu, Y., Montcouquiol, M., Zhou, L., Komatsu, K., Shi, D., Fujimori, T., Labeau, J., Tyteca, D., Courtoy, P., Poumay, Y., Uemura, T., and Goffinet, A. M. (2010) Lack of cadherins Celsr2 and Celsr3 impairs ependymal ciliogenesis, leading to fatal hydrocephalus. *Nat. Neurosci.* **13,** 700–707
7. Wong, K., Ren, X. R., Huang, Y. Z., Xie, Y., Liu, G., Saito, H., Tang, H., Wen, L., Brady-Kalnay, S. M., Mei, L., Wu, J. Y., Xiong, W. C., and Rao, Y. (2001) Signal transduction in neuronal migration. Roles of GTPase-activating proteins and the small GTPase Cdc42 in the Slit-Robo pathway. *Cell* **107,** 209–221
8. Wu, W., Wong, K., Chen, J., Jiang, Z., Dupuis, S., Wu, J. Y., and Rao, Y. (1999) Directional guidance of neuronal migration in the olfactory system by the protein Slit. *Nature* **400,** 331–336
9. Yang, Y., Marcello, M., Endris, V., Saffrich, R., Fischer, R., Trendelenburg, M. F., Sprengel, R., and Rappold, G. (2006) MEGAP impedes cell migration via regulating actin and microtubule dynamics and focal complex formation. *Exp. Cell Res.* **312,** 2379–2393
10. Guerrier, S., Coutinho-Budd, J., Sassa, T., Gresset, A., Jordan, N. V., Chen, K., Jin, W. L., Frost, A., and Polleux, F. (2009) The F-BAR domain of srGAP2 induces membrane protrusions required for neuronal migration and morphogenesis. *Cell* **138,** 990–1004
11. Soderling, S. H., Binns, K. L., Wayman, G. A., Davee, S. M., Ong, S. H., Pawson, T., and Scott, J. D. (2002) The WRP component of the WAVE-1 complex attenuates Rac-mediated signaling. *Nat. Cell Biol.* **4,** 970–975
12. Soderling, S. H., Guire, E. S., Kaech, S., White, J., Zhang, F., Schutz, K., Langeberg, L. K., Banker, G., Raber, J., and Scott, J. D. (2007) A WAVE-1 and WRP signaling complex regulates spine density, synaptic plasticity, and memory. *J. Neurosci.* **27,** 355–365
13. Kariya, S., Aoji, K., Akagi, H., Fukushima, K., Chikumoto, E., Ogawa, T., Karaki, M., and Nishizaki, K. (2000) A terminal deletion of the short arm of chromosome 3. Karyotype 46, XY, del(3) (p25-pter); a case report and literature review. *Int. J. Pediatr. Otorhinolaryngol.* **56,** 71–78
14. Roy, N. S., Benraiss, A., Wang, S., Fraser, R. A., Goodman, R., Couldwell, W. T., Nedergaard, M., Kawaguchi, A., Okano, H., and Goldman, S. A. (2000) Promoter-targeted selection and isolation of neural progenitor cells from the adult human ventricular zone. *J. Neurosci. Res.* **59,** 321–331
15. Gage, F. H. (2000) Mammalian neural stem cells. *Science* **287,** 1433–1438
16. Coskun, V., Wu, H., Blanchi, B., Tsao, S., Kim, K., Zhao, J., Biancotti, J. C., Hutnick, L., Krueger, R. C., Jr., Fan, G., de Vellis, J., and Sun, Y. E. (2008) CD133$^+$ neural stem cells in the ependyma of mammalian postnatal forebrain. *Proc. Natl. Acad. Sci. U.S.A.* **105,** 1026–1031
17. Doetsch, F., Caillé, I., Lim, D. A., García-Verdugo, J. M., and Alvarez-Buylla, A. (1999) Subventricular zone astrocytes are neural stem cells in the adult mammalian brain. *Cell* **97,** 703–716
18. Laywell, E. D., Rakic, P., Kukekov, V. G., Holland, E. C., and Steindler, D. A. (2000) Identification of a multipotent astrocytic stem cell in the immature and adult mouse brain. *Proc. Natl. Acad. Sci. U.S.A.* **97,** 13883–13888
19. Sanai, N., Tramontin, A. D., Quiñones-Hinojosa, A., Barbaro, N. M., Gupta, N., Kunwar, S., Lawton, M. T., McDermott, M. W., Parsa, A. T., Manuel-García Verdugo, J., Berger, M. S., and Alvarez-Buylla, A. (2004) Unique astrocyte ribbon in adult human brain contains neural stem cells but lacks chain migration. *Nature* **427,** 740–744
20. Bachoo, R. M., Maher, E. A., Ligon, K. L., Sharpless, N. E., Chan, S. S., You, M. J., Tang, Y., DeFrances, J., Stover, E., Weissleder, R., Rowitch, D. H., Louis, D. N., and DePinho, R. A. (2002) Epidermal growth factor receptor and Ink4a/Arf. Convergent mechanisms governing terminal differentiation and transformation along the neural stem cell to astrocyte axis. *Cancer Cell* **1,** 269–277
21. Holland, E. C., Celestino, J., Dai, C., Schaefer, L., Sawaya, R. E., and Fuller, G. N. (2000) Combined activation of Ras and Akt in neural progenitors induces glioblastoma formation in mice. *Nat. Genet.* **25,** 55–57
22. Sanai, N., Alvarez-Buylla, A., and Berger, M. S. (2005) Neural stem cells and the origin of gliomas. *N. Engl. J. Med.* **353,** 811–822
23. Stiles, C. D., and Rowitch, D. H. (2008) Glioma stem cells. A midterm exam. *Neuron* **58,** 832–846
24. Faiz, M., Acarin, L., Castellano, B., and Gonzalez, B. (2005) Proliferation dynamics of germinative zone cells in the intact and excitotoxically lesioned postnatal rat brain. *BMC Neurosci.* **6,** 26
25. Carlson, B. R., Lloyd, K. E., Kruszewski, A., Kim, I. H., Rodriguiz, R. M., Heindel, C., Faytell, M., Dudek, S. M., Wetsel, W. C., and Soderling, S. H. (2011) WRP/srGAP3 facilitates the initiation of spine development by an inverse F-BAR domain, and its loss impairs long term memory. *J. Neurosci.*

31, 2447–2460

26. Kuo, C. T., Mirzadeh, Z., Soriano-Navarro, M., Rasin, M., Wang, D., Shen, J., Sestan, N., Garcia-Verdugo, J., Alvarez-Buylla, A., Jan, L. Y., and Jan, Y. N. (2006) Postnatal deletion of Numb/Numblike reveals repair and remodeling capacity in the subventricular neurogenic niche. *Cell* **127,** 1253–1264

27. Kim, I. H., Park, S. K., Sun, W., Kang, Y., Kim, H. T., and Kim, H. (2004) Spatial learning enhances the expression of inositol 1,4,5-trisphosphate 3-kinase A in the hippocampal formation of rat. *Brain Res. Mol. Brain Res.* **124,** 12–19

28. Badea, A., Ali-Sharief, A. A., and Johnson, G. A. (2007) Morphometric analysis of the C57BL/6J mouse brain. *Neuroimage* **37,** 683–693

29. Arenkiel, B. R., Klein, M. E., Davison, I. G., Katz, L. C., and Ehlers, M. D. (2008) Genetic control of neuronal activity in mice conditionally expressing TRPV1. *Nat. Methods* **5,** 299–302

30. Goto, J., Tezuka, T., Nakazawa, T., Sagara, H., and Yamamoto, T. (2008) Loss of Fyn tyrosine kinase on the C57BL/6 genetic background causes hydrocephalus with defects in oligodendrocyte development. *Mol. Cell. Neurosci.* **38,** 203–212

31. Rolf, B., Kutsche, M., and Bartsch, U. (2001) Severe hydrocephalus in L1-deficient mice. *Brain Res.* **891,** 247–252

32. Zhang, W., Yi, M. J., Chen, X., Cole, F., Krauss, R. S., and Kang, J. S. (2006) Cortical thinning and hydrocephalus in mice lacking the immunoglobulin superfamily member CDO. *Mol. Cell. Biol.* **26,** 3764–3772

33. Utriainen, A., Sormunen, R., Kettunen, M., Carvalhaes, L. S., Sajanti, E., Eklund, L., Kauppinen, R., Kitten, G. T., and Pihlajaniemi, T. (2004) Structurally altered basement membranes and hydrocephalus in a type XVIII collagen-deficient mouse line. *Hum. Mol. Genet.* **13,** 2089–2099

34. Endo, M., Jain, R. K., Witwer, B., and Brown, D. (1999) Water channel (aquaporin 1) expression and distribution in mammary carcinomas and glioblastomas. *Microvasc. Res.* **58,** 89–98

35. McCoy, E., and Sontheimer, H. (2007) Expression and function of water channels (aquaporins) in migrating malignant astrocytes. *Glia* **55,** 1034–1043

36. Hayashi, Y., Edwards, N. A., Proescholdt, M. A., Oldfield, E. H., and Merrill, M. J. (2007) Regulation and function of aquaporin-1 in glioma cells. *Neoplasia* **9,** 777–787

37. Saadoun, S., Papadopoulos, M. C., Davies, D. C., Bell, B. A., and Krishna, S. (2002) Increased aquaporin 1 water channel expression in human brain tumours. *Br. J. Cancer* **87,** 621–623

38. Mendoza-Torreblanca, J. G., Martínez-Martínez, E., Tapia-Rodríguez, M., Ramírez-Hernández, R., and Gutiérrez-Ospina, G. (2008) The rostral migratory stream is a neurogenic niche that predominantly engenders periglomerular cells. *In vivo* evidence in the adult rat brain. *Neurosci. Res.* **60,** 289–299

39. Hatano, M., Eguchi, J., Tatsumi, T., Kuwashima, N., Dusak, J. E., Kinch, M. S., Pollack, I. F., Hamilton, R. L., Storkus, W. J., and Okada, H. (2005) EphA2 as a glioma-associated antigen. A novel target for glioma vaccines. *Neoplasia* **7,** 717–722

40. Wykosky, J., Gibo, D. M., Stanton, C., and Debinski, W. (2005) EphA2 as a novel molecular marker and target in glioblastoma multiforme. *Mol. Cancer Res.* **3,** 541–551

41. Ferguson, B., Matyszak, M. K., Esiri, M. M., and Perry, V. H. (1997) Axonal damage in acute multiple sclerosis lesions. *Brain* **120,** 393–399

42. Sakakibara, S., Nakamura, Y., Yoshida, T., Shibata, S., Koike, M., Takano, H., Ueda, S., Uchiyama, Y., Noda, T., and Okano, H. (2002) RNA-binding protein Musashi family. Roles for CNS stem cells and a subpopulation of ependymal cells revealed by targeted disruption and antisense ablation. *Proc. Natl. Acad. Sci. U.S.A.* **99,** 15194–15199

43. Kuhn, H. G., Winkler, J., Kempermann, G., Thal, L. J., and Gage, F. H. (1997) Epidermal growth factor and fibroblast growth factor-2 have different effects on neural progenitors in the adult rat brain. *J. Neurosci.* **17,** 5820–5829

44. Ohmiya, M., Fukumitsu, H., Nitta, A., Nomoto, H., Furukawa, Y., and Furukawa, S. (2001) Administration of FGF-2 to embryonic mouse brain induces hydrocephalic brain morphology and aberrant differentiation of neurons in the postnatal cerebral cortex. *J. Neurosci. Res.* **65,** 228–235

45. Holland, E. C., Hively, W. P., DePinho, R. A., and Varmus, H. E. (1998) A constitutively active epidermal growth factor receptor cooperates with disruption of G_1 cell cycle arrest pathways to induce glioma-like lesions in mice. *Genes Dev.* **12,** 3675–3685

46. Craig, C. G., Tropepe, V., Morshead, C. M., Reynolds, B. A., Weiss, S., and van der Kooy, D. (1996) *In vivo* growth factor expansion of endogenous subependymal neural precursor cell populations in the adult mouse brain. *J. Neurosci.* **16,** 2649–2658

47. Del Bigio, M. R. (2004) Cellular damage and prevention in childhood hydrocephalus. *Brain Pathol.* **14,** 317–324

48. Kanno, S., Abe, N., Saito, M., Takagi, M., Nishio, Y., Hayashi, A., Uchiyama, M., Hanaki, R., Kikuchi, H., Hiraoka, K., Yamasaki, H., Iizuka, O., Takeda, A., Itoyama, Y., Takahashi, S., and Mori, E. (2011) *J. Neurol.* **11,** 1949–1957

49. Weller, R. O., and Williams, B. N. (1975) Cerebral biopsy and assessment of brain damage in hydrocephalus. *Arch. Dis. Child.* **50,** 763–768

50. Hattingen, E., Jurcoane, A., Melber, J., Blasel, S., Zanella, F. E., Neumann-Haefelin, T., and Singer, O. C. (2010) Diffusion tensor imaging in patients with adult chronic idiopathic hydrocephalus. *Neurosurgery* **66,** 917–924